Surface Functionalised Graphene for UV-Visible Photon Detection

Nathan D. Cottam, Jonathan S. Austin, Feiran Wang, Jonathan Gosling, Mark Fromhold, Chris Tuck, Richard Hague, Amalia Patanè, Lyudmila Turyanska and Oleg Makarovsky
University of Nottingham
Nottingham, NG7 2RD
UNITED KINGDOM

nathan.cottam1@nottingham.ac.uk; Lyudmila.Turyanska@nottingham.ac.uk

ABSTRACT

Exploitation of the unique electronic properties of graphene and its compatibility with surface functionalisation offers a platform for an expansive range of applications in electronics and optoelectronics. By capping the graphene layer with another material or nanostructure such as PbS quantum dots the photoresponsivity can be enhanced to $> 10^9$ AW^{-1} in the visible (VIS) to near infrared range. Recent progress in the synthesis of high stability inorganic perovskite nanocrystals (NCs) has led to their increasing use in broadband photodetectors. These NCs are of particular interest for the UV range as they have the potential to extend the wavelength range of photodetectors based on traditional materials. We demonstrated a defect-assisted high photoresponsivity ($R > 10^6$ AW^{-1} in the UV-VIS range) in graphene transistors decorated with all-inorganic caesium lead halide perovskite NCs. Advances in additive manufacturing and inkjet printing enabled us to formulate printable graphene and perovskite NC inks and fabricate partially and fully printed UV-VIS photosensors with high photoresponsivity, reaching $> 10^6$ AW^{-1} for partially printed graphene/perovskite detectors and 20 AW^{-1} for fully printed.

Keywords: graphene, perovskite, quantum dot, inkjet printing, photodetector.

1.0 INTRODUCTION

Single layer graphene (SLG) is an excellent platform for nanoscale optoelectronic applications. Described as a zero bandgap semiconductor, its unique band structure gives rise to many interesting properties including ambipolar electric field effect [1], tuneable charge carrier density [2] and high carrier mobility [3]. Graphene itself is photosensitive over a wide range of wavelengths from ultraviolet (UV) to THz [4] with ultrafast response time (~ 1 ps) [5], but has very low absorption (~ 2%) and photoresponsivity ($R < 0.001AW^{-1}$) [5]. Surface functionalisation of single layer graphene (SLG) with optically active materials is a novel route to controlled fabrication of high sensitivity photodetectors in the UV, visible (VIS) and near infrared (NIR) [6], [7]. Realisation of graphene-based UV-VIS-NIR photodetectors was demonstrated with devices ranging from vertical tunnel diodes to *p-n* junctions and hybrid planar devices [8], [9].

Here, we demonstrate that the choice of materials for the surface layer offers opportunities for selecting and tailoring the photosensitivity range from the NIR with semiconductor QDs [10] to the VIS [11] and UV range [12] with perovskite nanocrystals (NCs). Of particular interest is surface decoration of graphene with perovskites owing to their extraordinary optical properties, including strong optical absorption, high quantum yield (QY) and widely tuneable band gap energy [13]. All-inorganic lead halide perovskite NCs with chemical composition $CsPbX_3$ (where X = Cl, Br, I or mixed) have attracted substantial attention due to their enhanced stability over organic counterparts [14]. The choice of capping ligand offers a tool to further improve the environmental stability of the perovskites [15] and to control charge dynamics at the graphene – perovskite interface [16]. The spectral response of the surface decorated graphene detector is determined by the perovskite absorption profile, which can be modified by the NC chemical composition. By changing the halide content from iodine to a bromine/chlorine mix the band gap emission of the NCs is tuned from 680

nm to ~460 nm. UV selective photoresponse was achieved by fabricating graphene devices decorated with CsPb(Br/Cl)$_3$ NCs and achieved responsivity of $R > 10^6$ AW^{-1} at 250nm excitation wavelength [12].

Our studies revealed that performance of these devices is governed by the charge transfer between the perovskite NCs and graphene, and charge carrier transport within the graphene layer. A defect-assisted high photoconductive gain was observed across the UV-VIS range in SLG field effect transistors (FETs) functionalised with CsPbI$_3$ NCs [11], arising from the efficient transfer of photo-generated electrons from the NCs to SLG and a long lifetime (~1 s) of photo-generated holes that are trapped in the NC, enabling high photoresponsivity, $R > 10^6$ AW^{-1}. We found that slow charging of the NCs causing anomalously large hysteresis in the gate voltage dependence, V_g, of the conductivity, σ, of the graphene channel. The temperature dependent studies of both the electric field hysteresis and optical response indicated a Pb defect related deep ~0.3 eV trap state responsible for the charge trapping. A phenomenological 2-capacitor model was developed [11] to describe the behaviour observed in these hybrid perovskite/graphene FETs [11], as the traditional parallel plate capacitor model for graphene FETs could not be applied to this type of devices.

To explore opportunities for upscaling the fabrication of graphene photon detectors and their manufacturing on flexible substrates, we employ an inkjet printing additive manufacturing (AM) method to low dimensional materials such as graphene flakes and perovskite NCs. Perovskite NC inks were formulated and deposited using inkjet printing to produce a photosensitive layer onto a SLG device, with photoresponsivity reaching, $R \sim 10^7$ AW^{-1} in the UV-VIS spectral range for CsPb(Br/I)$_3$/graphene devices [17], exceeding that achieved for our drop-cast perovskite/SLG FETs. Ink formulations of graphene (iGraphene) are also considered to replace conventional SLG graphene detectors. In contrast to SLG, transport properties of iGraphene are strongly affected by the formation of graphene networks and depend on the film morphology and a number of additional parameters, such as packing fraction of graphene flakes, resistance and capacitance of flake-to-flake junctions [18]. Our fully inkjet-printed iGraphene/CsPb(Br/I)$_3$ devices demonstrated responsivity of $R > 20$ AW^{-1}, which can be improved by optimising ink compositions and device geometries. Furthermore, iGraphene offers a novel route to Ohmic electrode formation on other low-dimensional van der Waals (vdW) materials such as InSe and GaSe, where traditional metal contacts (e.g. Au) typically form Schottky junctions. Our InSe/graphene devices, produced using a combination of mechanical exfoliation/stamping and inkjet printing, display broadband UV-NIR spectral response with high on/off ratio (~10^3) and sub-millisecond response times, $\tau < 0.4$ ms.

2.0   APPROACH

2.1   Materials and Device Fabrication

In these devices we utilised chemical vapour deposition (CVD) grown single layer graphene (SLG) and SLG/hBN heterostructures on 285 nm SiO$_2$/Si substrates from multiple sources including Graphene Supermarket [19] and colleagues from CNI@NEST [20]. The 0D/2D devices were fabricated using a combination of electron beam lithography and liquid deposition of nanocrystals (NCs) in two different planar geometries: a multiterminal Hall bar and a planar diode with a short channel length. The Hall bar geometry is used for magneto-transport measurements, enabling the precise measurement of carrier concentration and mobility (Hall effect and 4-terminal conductivity measurements). The short two-terminal diodes are used for measurements of photocurrent and photoresponsivity with a short electron transit time and reduced edge effects due to a smaller number of carrier traps at the edges of 2D layers.

0D materials such as PbS QDs and CsPbX$_3$ NCs are used for surface functionalisation. PbS QDs were synthesised following protocol described in Ref. [10]. CsPbX$_3$ NCs were synthesised via the hot-injection method with improved properties by post-synthesis replacement of oleic acid ligands with iminodibenzoic acid as outlined in Ref. [15]. The NCs have a long shelf life in solution (>2 months), are stable under different environmental conditions, and have a high quantum yield of up to 90% in the visible spectral range.

2.2   Inkjet Deposition

The ink used to deposit iGraphene was purchased from Sigma-Aldrich (product number: 793663). The ink contains liquid exfoliated graphene flakes with an average size of 2590 nm^2 and ethyl cellulose (EC) with a 2.4 wt% solids concentration; dispersed in an 85:15 mixture of cyclohexanone/terpineol to provide a suitable rheology for jetting. The ink had a density of 9.665 g cm^{-3}, surface tension of 33 mN m^{-1}, and viscosity of 11.3 mPa·s at room temperature. CsPbX$_3$ NC inks were formulated for inkjet printing by dispersing 5 mg ml^{-1} CsPbX$_3$ NCs in a mixture of hexane, cyclohexanone, and terpineol (1:3:1 v/v) and sonicating for 30 minutes at room temperature. All inks were stored in Fujifilm Dimatix cartridges at room temperature. Graphene ink cartridges were stored in ambient conditions, and perovskite-based ink cartridges were stored under a N$_2$ atmosphere.

Films were printed on Si/SiO$_2$ and on flexible Kapton substrates using a drop-on-demand (DoD) piezo-driven Fujifilm Dimatix DMP-2800 inkjet printer. In each print, a single nozzle was used to deposit single lines in the x-direction sequentially. To print additional layers, this process was repeated directly on top of the previous layer. The morphology of printed films is dictated by the drop spacing, which is the distance between the centres of neighbouring drops deposited by the printer. For the perovskite NC inks, printing was performed with Fujifilm Dimatix Samba cartridges with a 2.4 pl drop volume and nozzle diameter 17 μm, which formed printed spots with a diameter of ~40 μm on Si/SiO$_2$. Perovskite NCs were deposited with a drop-spacing of 20 μm at a substrate temperature of 60 °C in N$_2$ atmosphere. A leader bar (a small redundant bar printed to the left of prints) was used for all prints to ensure favourable jetting at the beginning of each printed swath. The iGraphene printed films were annealed in a vacuum (~1 mbar) oven at 250 °C for 30 min.

2.3   Morphological, Optical and Electrical Characterisation

Transmission electron microscopy (TEM) images were acquired on a JEM-2100F, JOEL operated at 200 kV and were analysed using ImageJ for nanoparticle size measurements. Optical properties were assessed by photoluminescence spectroscopy studies, which were conducted using a Horiba Jobyn Yvon micro-PL system, equipped with a frequency-doubled Nd: YVO4 laser (λ_{ex} = 532 nm), HeNe laser (λ_{ex} = 633 nm), and Si charge-coupled device (CCD) camera. The optical absorption spectra were measured using an Edinburgh Instruments FLS980 fluorescence spectrometer equipped with an integrating sphere module. Electrical measurements and photocurrent measurements were performed using Keithley-2400 Source-Meters and Keitheley-2010 multimeters in DC mode. Fixed wavelength excitations were provided by a set of six fibre-coupled diode-pumped solid state diode pumped solid state lasers with calibrated output power $\leq$ 30 mW for all output wavelengths (λ_{ex} = 405, 450, 530, 635, 808, 1060 nm). A deuterium lamp equipped with a short-pass filter was used as a UV (250 nm) source. A MicroHR monochromator (Horiba, MHRA-2X-FS, with 75 W xenon source) was used for photocurrent measurements under tuneable wavelength (λ_{ex} = 200 nm to 1000 nm). Photoresponsivity (R) was calculated by $R = I_{pc}/P_{inc}$ where I_{pc} is the maximum change in source-drain current (I_{sd}) recorded after constant illumination and P_{inc} is the total light power incident on the sample.

2.4   Magneto-Transport and Quantum Hall Effect

Experimental measurements in constant and slow-changing magnetic fields were performed in a closed-cycle 16 T superconducting solenoid system (Cryogenics Ltd), which includes a cryostat temperature control inset (1.5 K < T < 400 K). For magnetic field-dependent studies, the field sweep rate of $\approx$ 0.005 T s^{-1} was used. DC voltage-current dependences were measured using Keithley-2400 SourceMeter units. Cyclic gate voltage, V$_g$, and sweeps were performed using a constant sweep rate of about 0.1 V s^{-1}.

Pulsed magnetic field measurements were performed up to $B \leq$ 60 T, field sweep rate ~1000 T s^{-1}. The pulsed magnetic fields are created by discharging a capacitor through a liquid nitrogen-cooled resistive coil in a short time ($\approx$ 100 ms). The sample was placed in a helium-cooled cryostat and measured in the temperature range 4 K < T < 300 K. A constant DC voltage was applied to a Hall bar sample with either

constant applied V_g or cyclic V_g sweeps. The values of longitudinal and transverse voltages were amplified by Stanford SR560 low noise amplifiers and measured using a fast multichannel PXI acquisition system (National Instruments). Parasitic voltages generated during the fast changes of the field were compensated using analysis of the data obtained during field-up and field-down branches of the magnetic pulse.

3.0 RESULTS AND DISCUSSION

3.1 Surface Decoration of Graphene with 0D Materials for Spectral Selectivity of Detectors

Colloidal quantum dots (QDs) are of particular interest for VIS-NIR detection as their optical properties can be fine-tuned by varying their size and/or composition [21]. Here, we investigated the properties of single layer graphene (SLG) functionalised with an overlayer of near-infrared PbS colloidal QDs (Figure 1a). QDs with an average PbS core diameter of $d_{QD} = 4.5$ nm (Figure 1b) were stabilised using the following capping ligands of different length, l, which determines the effective separation between the PbS nanocrystals and graphene: polyethylene glycol H-(O-CH$_2$-CH$_2$)$_n$-OH with $n = 2000$ for QD$_{p2000}$ and $n = 500$ for QD$_{p500}$ [22] and corresponding length of $l \approx 10$ nm and $l \approx 5$ nm, respectively; a mixture of thioglycerol (TGL) and 2,3-dimercapto-1-propanol (DTG), $l \approx 0.5$ nm for QD$_{TGL}$ [23]. The QDs were drop-cast from aqueous solution (5 mg mL^{-1}) to produce continuous thick (> 100 nm) coverage of the graphene layer, followed by drying for 12 h in vacuum at room temperature. The size of the QDs and their room temperature photoluminescence spectra (with a peak at photon energy ≈ 1.1 eV) are similar in all three structures, i.e., they are not affected by the ligands.

We demonstrated that the polarity of the conductivity and the carrier concentration of SLG can be modified, and photoresponsivity of SLG can be significantly enhanced by the choice of ligands on the QDs. By reducing the length of capping ligands, hence the thickness of the dielectric barrier between the QDs and the SLG, and by preserving the integrity of the ligand layer, we achieved efficient transfer of photogenerated carriers from the QDs to the graphene before recombining, resulting in enhanced responsivities of up to $R \approx 10^9$ AW^{-1} for SLG decorated with QD$_{TGL}$ (Figure 1c).
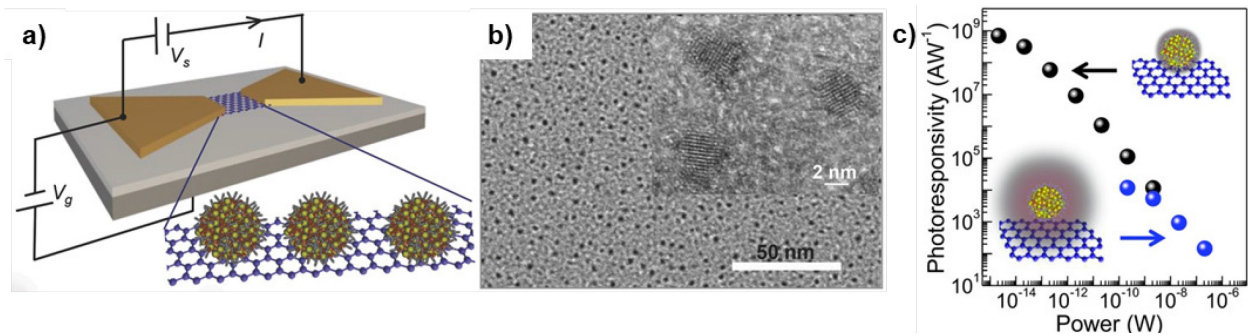
Figure 1: a) Schematic diagram of the device and circuit arrangement. b) TEM and high resolution TEM (inset) images of QDs (QD$_{p500}$) deposited on a graphene oxide TEM support film. c) Photoresponsivity versus incident power for QD$_{TGL}$/SLG (black) and QD$_{p500}$/SLG (blue) devices under λ_{ex} = 514 nm illumination. Figure reproduced with permission from Ref. [10].

In these quantum dot decorated graphene devices the high responsivity results from a photoconductive gain mechanism described by the following expression,

$$R = \frac{\alpha e}{h\nu} \frac{\tau_{QD}}{\tau_{trans}} .$$

(1)

Here $\alpha = \alpha_i s$ is the absorbance of the PbS QDs, where α_i is the absorption coefficient and s is the thickness of the QD layer, τ_{QD} is the lifetime of photogenerated charge on the QD, τ_{trans} is the electron transit time in SLG, h is Planck's constant, e is electron charge and v is the frequency of excitation light. τ_{QD}/τ_{trans} is referred to as the gain coefficient and typically $\tau_{QD} \gg \tau_{trans}$ resulting in the observed high photoresponsivity for decorated graphene photosensors [10].

To target the UV-VIS detection range we used all-inorganic caesium lead halide ($CsPbX_3$, X = Cl, Br, I or mixed) perovskite NCs (Figure 2) synthesised following the procedure outlined in Ref. [15]. The stability of $CsPbX_3$ NCs is affected by the strength of binding, surface density and stability of the capping molecules. Oleic acid (OA), oleylamine (OLA), and trioctylphosphine oxide (TOPO) are commonly used as capping ligands [24], but fail to prevent the degradation of the NCs over time. On the other hand, bidentate ligands, such as iminodibenzoic acid (IDA) and didodecyldimethylammonium bromide (DDAB), can improve the NC stability due to their coordination to two sites on the NC surface and a stronger steric effect [25], [26]. Our NC synthesis incorporates a ligand exchange reaction to replace OA and OLA ligands with IDA, resulting in a significant increase in their shelf-life (> 2 months) and quantum yield (QY > 90%), and improved stability under different environmental conditions [15].

The NCs form small cubic structures (Figure 2a), measured using transmission electron microscopy (TEM), of varying average size, which is dependent on chemical composition and reaction parameters [15]. For example, the $CsPbI_3$ NCs used in this work have an average size of 12.9 ± 1.7 nm, whereas our $CsPb(Br/Cl)_3$ NCs have an average size of 16 ± 3 nm. The bandgap, absorption profile and photoluminescence (PL) emission can be controlled through the halide content of the NCs from 680 nm to 520 nm and 460 nm emission for $CsPbI_3$, $CsPbBr_3$ and $CsPb(Br/Cl)_3$, respectively (Figure 2b), but can be tuned between these values by further modification of halide content and ratio [14]. The NCs are deposited onto CVD-grown graphene via a drop-casting method (Figure 2a). The SLG is typically placed on a SiO_2/Si substrate with SiO_2 layer thickness of 285 nm to form a field effect transistor (FET); some devices use monolayer hBN between the SLG and SiO_2 in order to improve SLG properties.
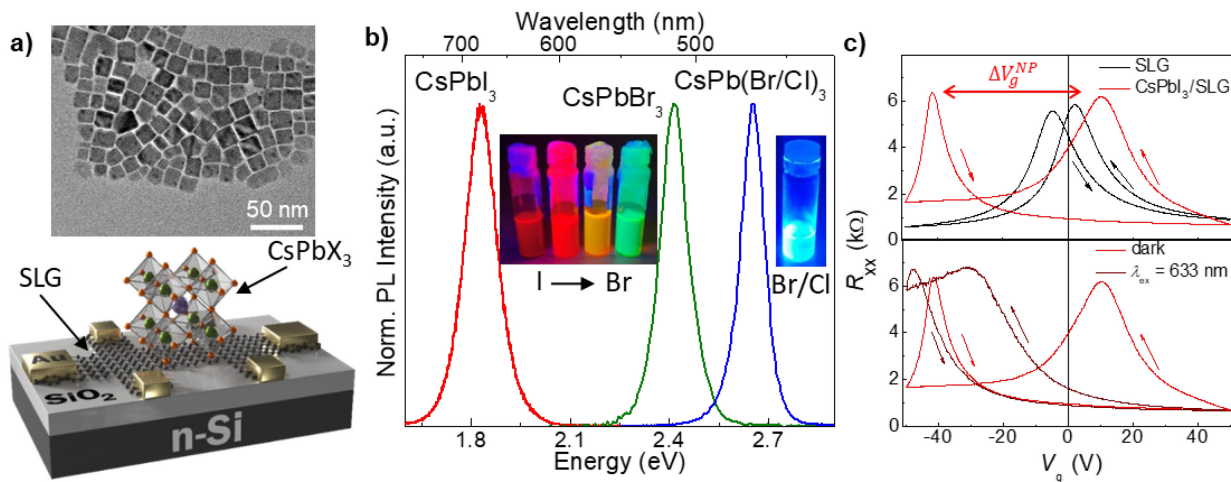

Figure 2: a) Top: TEM image of drop-cast cubic CsPbI₃ NCs. Bottom: Schematic diagram of a hybrid perovskite NC/SLG device. b) PL spectra and images under UV light (λₑₓ = 365 nm) of CsPbX₃ NCs with different halide content synthesised for this work. b) Top: dependence of resistance on applied gate voltage for SLG (black) and hybrid CsPbI₃/SLG (red). Bottom: hybrid CsPbI₃/SLG device in the dark (red) and under illumination (maroon) with λₑₓ = 633 nm laser light (P = 310 W/m²). Arrows indicate direction of the Vg sweeps, sweep rate = 0.3 V/sec, T = 295 K. Figure reproduced with permission from Ref. [11].

The gate voltage characteristics of FETs based on pristine graphene and the $CsPbI_3$-decorated graphene are compared in Figure 2c. Pristine SLG devices typically have a resistance maximum (charge neutrality point) close to $V_g = 0$ V and exhibit only a small hysteresis loop, which we quantify in terms of the difference in the gate voltage value at charge neutrality (Dirac) point, $\Delta V_g^{NP} = 5$ V, between the forward (from negative to positive bias) and reverse sweeps of V_g. The pristine SLG device used here has a low electron carrier concentration of n $\approx 2 \times 10^{11}$ cm^{-2} at $V_g = 0$ V and carrier mobility $\mu_e \approx 6000$ cm^{2}V^{-1}s^{-1} at room temperature. Deposition of the perovskite NCs leads to a significant increase of the hysteresis of the graphene charge neutrality point V_g^{NP}, from $\Delta V_g^{NP} = 5$ V to $\Delta V_g^{NP} = 60$ V, which is dependent on gate voltage sweep range, sweep rate and temperature [11]. This effect is due to charge accumulation in the perovskite NCs directly adjacent to SLG. Our measurements confirm that a film of perovskite nanocrystals has resistance >10 GΩ, which is not affected by applied gate voltage and/or exposure to light [11] We note that the hysteresis is reproducible and device performance is fully reversible. Studies of the temperature dependence of this hysteresis effect revealed an activation energy $E_x \sim 0.3$ eV indicating a Pb-related deep trap state is responsible for the charge trapping, see Ref. [11]. In order to explain the hysteretic behaviour of the perovskite-graphene device we developed a phenomenological model, which expands the traditional field effect model (1C model) used to describe graphene FETs and treats the perovskite NCs as a second capacitor layer (2C model) in which a high density of charge is accumulated, see Ref. [11] for details.

The charge transfer is also affected by exposure to light as we observed a significant reduction of the hysteresis under light illumination, with V_g^{NP} remaining in the negative V_g region (Figure 2c). This behaviour can be explained by the effect of light on the gate-induced charge trapped in the perovskite NCs. The light generates electron–hole pairs in the NCs and the photoexcited electrons are quickly transferred to the SLG, while the less mobile photoexcited holes remain trapped in the NCs. This difference in relaxation times of photoexcited electrons and holes leads to the asymmetry of the $R_{xx}(V_g)$ shown in Figure 2c. We assume that photoexcited holes can recombine with gate-induced negative charges in the perovskite NCs. The V_g dependence of the resistance indicates the transfer of both photoexcited electrons and holes for $V_g < 0$ V, and the preferential transfer of photoexcited electrons for $V_g > 0$ V [11].

The SLG/perovskite devices are photosensitive over the wavelength range of optical absorption of the used NCs. Also, a large photocurrent is observed in the UV region ($\lambda < 400$ nm). Pristine graphene has a small optical absorbance ($\sim 2\%$) and consequently its photoresponsivity is very low ($R < 0.001$ AW^{-1}). Hence, the optical response of these hybrid perovskite NC/SLG devices is predominantly due to the optical absorption of the perovskite NCs and by the charge transfer between the NC layer and graphene. The SLG devices decorated with both types of perovskite NCs ($CsPbBr_3$ and $CsPbI_3$) have very high photoresponsivity of $R > 10^6$ AW^{-1} for all excitation wavelengths measured in the UV-VIS range ($250 - 633$ nm) at room temperature (Figure 3a). The highest photoresponsivity, $R \approx 5 \times 10^6$ AW^{-1}, is observed in the low power limit where the photocurrent approaches the noise equivalent power, NEP $\approx 10^{-14}$ W. The temporal response of the device following optical excitation is shown in Figure 3b. The observed exponential decay of the resistance has characteristic times of ~ 1 s. The relatively large ratio of the lifetime of the photoexcited holes trapped in the NCs, typically $\tau_{NC} > 1$ s and the electron transit time in graphene channel, $\tau_e < 1$ ns, give rise to high photoresponsivity ($R > 10^6$ AW^{-1} at $T = 295$ K) due to high photoconductive gain, see Equation (1).

Hybrid perovskite-graphene photodetectors were also fabricated for UV-specific sensing using 'blue' $CsPb(Br/Cl)_3$ NCs with an optical absorption edge/band gap at ~ 460 nm. These NCs were synthesised with slightly different ligands (OA, OLA and bromophenylmethyl (BPM)), but displayed similar transport characteristics and charge dynamics to the previously studied perovskite NCs. The blue perovskite decorated graphene maintained high responsivity, $R > 10^6$ AW^{-1}, with response time ~ 10 s in the UV ($\lambda_{ex} = 365$ nm) range (Figure 3c).
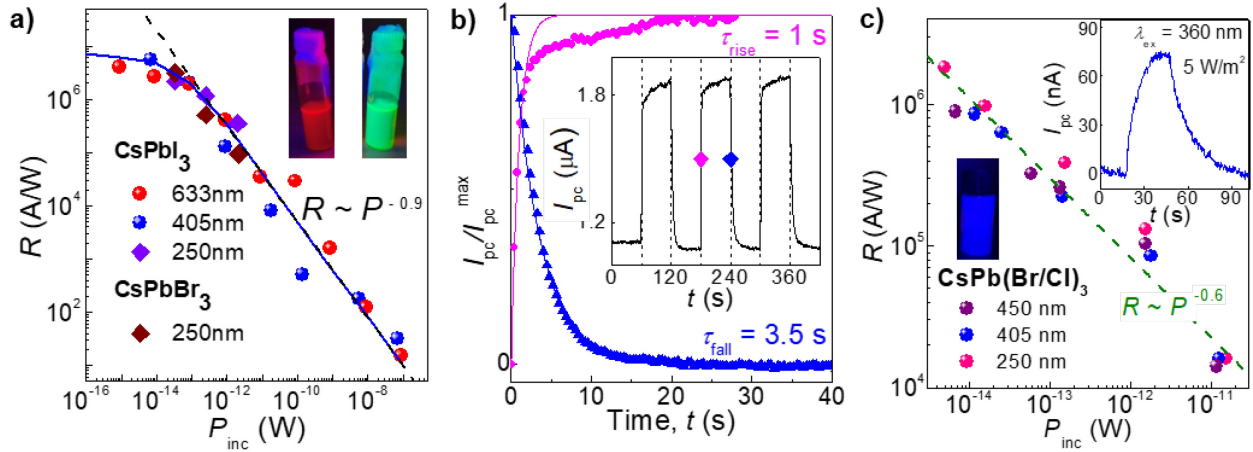
Figure 3: a) UV-Vis photoresponsivity of CsPbI₃/SLG and CsPbBr₃/SLG devices at λ_{ex} = 633, 405 and 250 nm. The dashed line is a fit using $R \sim P^{-0.9}$. The blue line is a guide to the eye. Inset: bottles of CsPbI₃ (red) and CsPbBr₃ (green) NCs in solution under UV (λ_{ex} = 365 nm) excitation. **b)** Temporal response of the photocurrent on rising and falling slope (ON/OFF) at point indicated by magenta (ON) and blue (OFF) points in the inset for the CsPbI₃/SLG device. Inset: light on/off time dependence of the photocurrent for the CsPbI₃/SLG device at T = 295 K (V_{sd} = 20 mV, V_g = 0 V, P = 325 W/m2, λ_{ex} = 633 nm). **c)** Responsivity of a CsPb(Br/Cl)₃/SLG device versus optical power, P_{inc}, under excitation with 250 nm, 405 nm, and 450 nm. Inset (right) shows a typical temporal response of the photocurrent under excitation with 360 nm and power density of 5 W/m². Inset (left) shows a bottle of CsPb(Br/Cl)₃ NCs in solution under UV (λ_{ex} = 365 nm) excitation. Figure a-b reproduced with permission from Ref. [11] and c from Ref. [12].

We found that the performance (responsivity, response time, etc.) of these devices is rather independent of the perovskite composition, whilst the spectral photoresponse mirrors the absorption profile of the NCs and can be tuned in a wide UV-Visible range.

3.2 Probing Charge Transport in Perovskite/Graphene Transistors with High Magnetic Fields

To enable translation of these research findings into industry, complete fundamental understanding of the phenomena underlying device performance is needed. Hence, we investigated the charge transfer processes in these perovskite/graphene heterostructures in high electric and magnetic fields (up to B=60 T) and at different temperatures, T [12]. Quantum Hall effect (QHE) was also observed in this system at low temperatures ($T < 100$ K) indicating that deposition of the NCs does not disrupt the quantum properties of SLG in low temperatures (Figure 4a). Magneto-transport experiments at high temperature ($T > 200$ K) in slowly changing (~ 0.005 T/s) and pulsed (~ 1000 T/s) magnetic fields revealed pronounced hysteresis effects (Figure 4b) in the transfer characteristics of the FET described by an associated magnetic charging time ($\tau_{mag} \sim 500$ s) for the CsPb(Br/Cl)₃ NCs. A unique measurement technique was developed at these high temperatures in order to measure the dynamics of Hall carrier concentration at different points on the $\sigma(Vg)$ hysteresis curve (Figure 4c) using relatively small ($B = 6$ T) magnetic field pulses (τ_{pulse}<100 ms), see Ref. [12]. These studies are key to further understanding the charge transfer mechanism at the graphene - perovskite interface and within the perovskite NCs themselves and helped to provide further evidence for our developed 2C model [12].
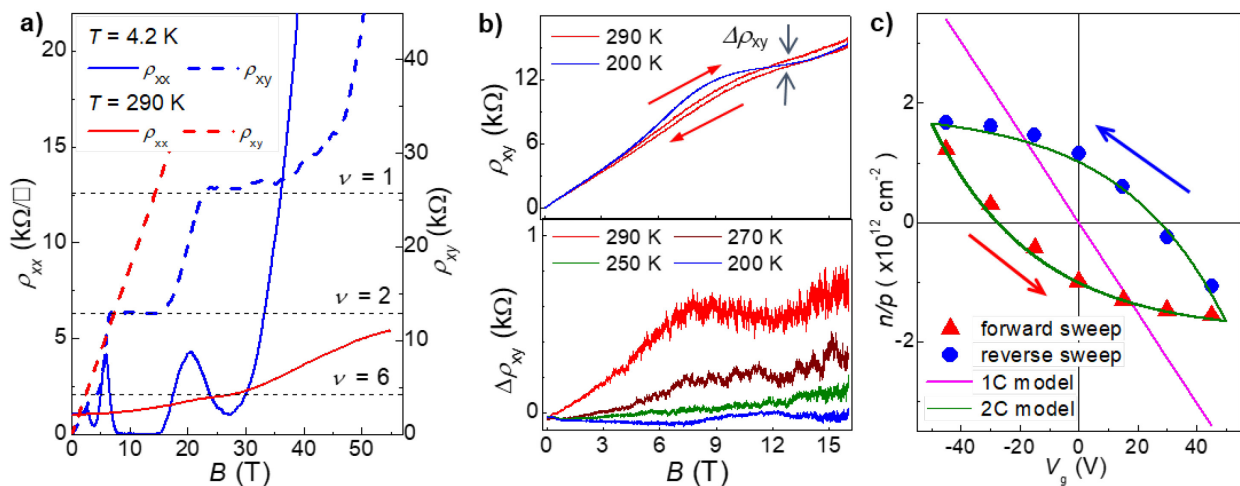
Figure 4: a) Longitudinal (solid lines), ρ_{xx}, and transverse (dashed lines), ρ_{xy}, magnetoresistance at zero gate voltage, $V_g = 0$, $T = 4.2$ K (blue) and 290 K (red). Dashed black lines show positions of the QHE plateau with Landau index $\nu = 1$, 2 and 6. b) Measurements of Sample 2 in slow magnetic field. a) Top: transverse magnetoresistance $\rho_{xy}(B)$ at $T = 290$ K (red) and $T = 200$ K (blue), sweep rate $\sim$0.005 T/s with 2 hour wait at $B = 16$ T field before the down field sweep. The amplitude of the hysteresis $\Delta\rho_{xy}$ in $\rho_{xy}(B)$ is observed at $T = 290$ K between up and down field sweeps. Bottom: $\Delta\rho_{xy}(B)$ curves measured at different temperatures. c) Time dependence of ρ_{xx} after a magnet quench. The red dash line is an exponential fit to the data. Inset: log scale fit of the normalised conductivity $\sigma = 1/\rho_{xx}$ by $\sigma \sim \exp(-t/\tau_{mag})$ with $\tau_{mag} = 540$ s. Figure reproduced with permission from Ref. [12].

3.3   Inkjet-Printed Graphene-Based Photosensors

$CsPbBr_3$ and $CsPb(Br/I)_3$ NCs were formulated into inks and deposited onto a CVD-grown graphene FET, $SLG/SiO_2/Si$, by inkjet printing to fabricate $CsPb(Br/I)_3/SLG$ and $CsPbBr_3/SLG$ devices. The gate voltage, V_g, dependence of SLG resistivity before and after deposition of $CsPb(Br/I)_3$ NCs revealed a large hysteresis and n-type shift of the charge neutrality point similar to previous drop-cast perovskite/SLG devices. Thus, indicating that inkjet deposition produces devices with similar transport properties to previous drop-cast perovskite NC devices. In the $CsPbX_3/SLG$ devices, the onset of photoresponse was observed at an excitation wavelength, $\lambda_{ex} = 600$ nm for $CsPb(Br/I)_3$ and $\lambda_{ex} = 520$ nm for $CsPbBr_3$ (Figure 5a), corresponding to the band gap of the perovskite NCs. After illumination, the electrical properties of the devices recover to $\sim 90\%$ of the original value in about a minute, however the full recovery can take up to several hours for large incident illumination powers, which is likely due to the charge trapping on NC surface defects and slow charge dynamics.

For both devices, the relationship between incident light power, P_{inc}, and the responsivity, R, follows $R \sim P^{-0.7}$ (Figure 5b), similar to the $R(P)$ for previous SLG devices decorated with perovskite NCs. However, a much greater maximum photoresponse was observed for the $CsPb(Br/I)_3$ device ($R = 4 \times 10^6$ AW^{-1}) than by the $CsPbBr_3$ device ($R = 7 \times 10^3$ AW^{-1}). The difference in photoresponsivity of the photodetectors decorated with different perovskite NCs is due to the NC composition, which affects their absorption and energy level alignment with SLG for charge transfer (inset in Figure 5b). Since higher levels of absorption at the used excitation energy (405 nm) and longer lifetimes of photoexcited trapped charges are observed for mixed halide $CsPb(Br/I)_3$ NCs, these devices have higher photoresponsivity compared to $CsPbBr_3$ NC decorated devices.
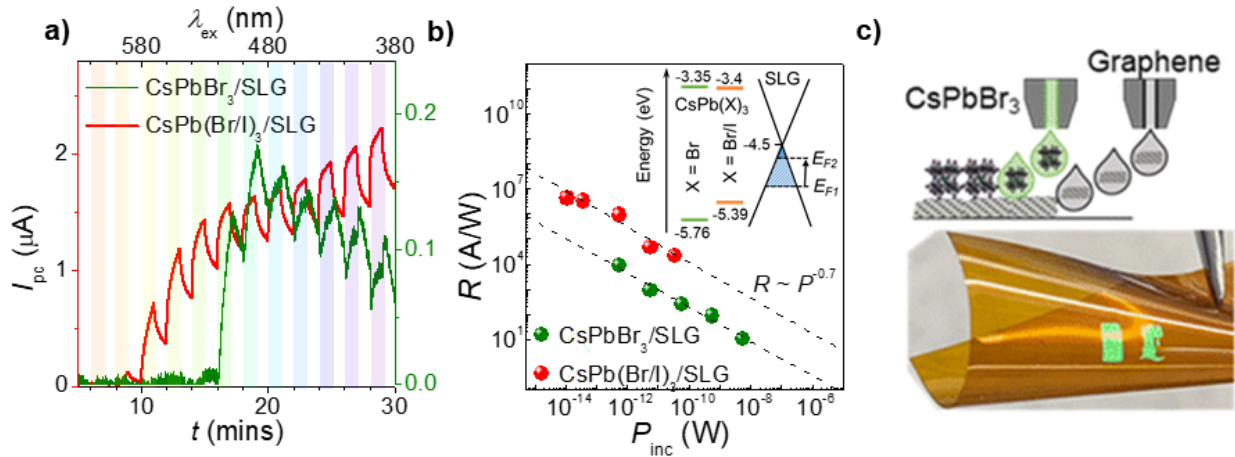
Figure 5: a) Dependence of photocurrent, I_{pc}, on the wavelength of incident light for the CsPb(Br/I)$_3$/SLG device (P ~ 0.03 W/m^2, V_{sd} = 10 mV) and the CsPbBr$_3$/SLG device (P ~ 0.3 W/m^2, V_{sd} = 5 mV). Shaded regions correspond to light on regime with wavelength corresponding to top axis b) Photoresponsivity of the same two devices as a function of illumination power measured after 1 minute illumination with λ_{ex} = 405 nm exposure (V_{sd} = 10 mV, V_g = 0 V). Inset: energy band diagram comparing CsPbBr$_3$ NCs, CsPb(Br/I)$_3$ NCs, and SLG. E_{F1} and E_{F2} denote the Fermi energy of the SLG device before (-4.6 eV) and after (-4.54 eV) CsPb(Br/I)$_3$ deposition, respectively. c) Top: schematic of inkjet printing process for a fully-printed hybrid CsPbBr$_3$-iGraphene heterostructure. Bottom: photograph of printed CsPbBr$_3$ NCs on a flexible Kapton substrate showing green photoluminescence under UV illumination. Figure reproduced with permission from Ref. [17].

We also successfully fabricated fully inkjet-printed CsPbBr$_3$/iGraphene heterostructure devices (Figure 5c) with a pair of Au contact pads printed using Au nanoparticle ink [27] onto Si/SiO$_2$ with a gap of ~ 30 μm. A single printed line of iGraphene was deposited across the gold electrodes and functionalised with inkjet-deposited CsPbBr$_3$ NCs. The CsPbBr$_3$/iGraphene device displayed a responsivity of 20 AW^{-1} [17] with a photoresponsivity threshold comparable to previous CsPbBr$_3$/SLG devices, as it is predominantly controlled by the absorption profile of the perovskite NCs. The different responsivities measured in perovskite decorated CVD graphene and iGraphene devices can be attributed to a large (over 3 orders of magnitude) decrease of carrier mobility, which results in longer transport times in iGraphene, as expected for graphene networks [18]. Additive manufacturing techniques such as inkjet printing for fabrication of devices enables the possibility of device fabrication on flexible substrates. Figure 5c demonstrates the inkjet printing of a patterned CsPbBr$_3$ NC structure on Kapton, showing photoluminescence under UV (λ_{ex} = 365 nm) illumination.

3.4   Inkjet-Printed Graphene Contacts for Low-Dimensional Materials

We demonstrate the use of iGraphene as an electrical contact material for low-dimensional van der Waals (vdW) materials. Here, we use a bulk flake of InSe (Area ~ 1 mm^2, thickness > 1 μm) and contacted it with iGraphene in a Hall bar style configuration (Figure 6a). The iGraphene makes good Ohmic (linear current-voltage) contacts to the InSe flake [18], which is typically difficult to achieve with conventional 3D materials such as metal films [28]. The absorption edge of bulk InSe at room temperature is ~ 1.1 eV (≈ 1130 nm) and these devices show a photoresponse at wavelengths below this value (Figure 6b). The photocurrent in the device, Ipc, increases at lower wavelengths due to the increased absorption of InSe at higher energies. A high photoresponsivity of 10^3 AW^{-1} was achieved for these devices (Figure 6c). Response times in these phototransistors are much faster than typical planar decorated graphene devices with fitted rise and fall times of < 1 ms (inset of Figure 6c). Incorporating different vdW materials could allow for tuning of the optical absorption of the device for wavelength specific detection.
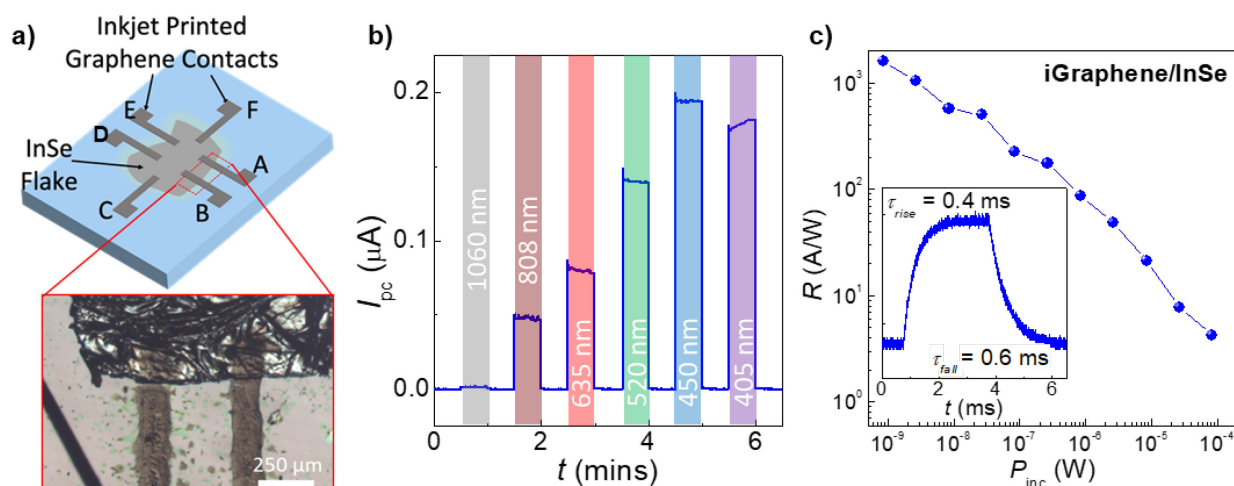
Figure 6: a) Representative schematic (top) and optical image (bottom) of an InSe phototransistor using inkjet-printed graphene contacts. b) Photocurrent versus time under illumination with different wavelengths of excitation laser light (P = 56 W m^{-2}, V = 1 V) as denoted by the coloured blocks (from left to right: 1080, 808, 635, 520, 450, 405 nm). c) Photoresponsivity versus incident power for an InSe phototransistor (V = 5 V, λ_{ex} = 405 nm). Inset shows typical response time characteristics of the devices (λ_{ex} = 405 nm, P = 280 W m^{-2}). Figure a reproduced with permission from Ref. [18].

4.0   CONCLUSIONS

In this paper we report a comprehensive study of surface functionalised graphene for photon detection in the UV-VIS-NIR range. We have studied CVD single layer graphene and inkjet-printed graphene functionalised by PbS quantum dots, CsPbX$_3$ nanocrystals and van der Waals semiconductor materials. We demonstrated that the characteristics of QD-decorated SLG devices are strongly affected by the properties of the QD capping layer, which acts as a dielectric barrier. The charge transfer from the QD layer and a corresponding accumulation of charge contribute to the strong photoresponse of the devices, while the presence of capping ligands affects the carrier mobility. We have demonstrated that a record high responsivity of 10^9 AW^{-1} in the visible range can be achieved for PbS/SLG heterostructures.

We have also achieved planar photon detectors by surface decoration of graphene with inorganic perovskite (CsPbX$_3$) nanocrystals. These detectors have stable performance and record high (>10^6 A/W) photoresponsivity in the UV–Vis (250–633 nm) range, with the spectral range of photoresponse controlled by the halide content of the NCs. We demonstrated that the performance of these devices is mediated by charge transfer at the PNC/graphene interface and depend on the applied electric field, temperature, incident light and magnetic field. For the first time, the effect of fast (< 100 ms) and slow quantizing magnetic fields on the charge transfer was studied and a characteristic magnetic time was introduced to describe the dependence of the charge transfer on the quantizing magnetic field. Our results demonstrate a means of modifying the electronic properties of CVD graphene sheets and the potential of hybrid QD-graphene layers in future optoelectronic devices, particularly for high sensitivity photodetection over an extended wavelength range.

The stability of the perovskites used and of the ink developed, enabled us to explore the potential of these inks as photosensitive layers in graphene-based photon detectors, including fully printed devices with responsivity R = 20 AW^{-1} in the UV range. Having a library of conductive (Au nanoparticle and graphene inks) and semiconducting (perovskite nanocrystals) materials, we achieved inkjet-manufactured photon detectors operational in the UV-VIS range with the highest photoresponsivity reported to date. Inkjet

deposition of low-dimensional materials, also allowed us to deposit graphene as an Ohmic contact material for UV-sensitive semiconducting van der Waals materials, which can be used to fabricate phototransistors with photoresponse controlled by the absorption profile of the chosen semiconductor material.

Overall, our work on a new generation of graphene-based photodetectors is useful for high sensitivity UV detection with potential applications in early missile detection systems, advanced communications in the UV and FET-based metrology. Incorporation of AM into device processing offers scalability and agility in device fabrication compatible with a wide range of substrate materials from conventional Si/SiO$_2$ and sapphire to flexible Kapton and even fabrics.

5.0   ACKNOWLEDGEMENTS

6.0   REFERENCES

[1]   A. K. Geim and K. S. Novoselov, "The rise of graphene," *Nat Mater*, vol. 6, no. 3, pp. 183–191, Mar. 2007, doi: 10.1038/nmat1849.

[2]   Y. Zhu *et al.*, "Graphene and Graphene Oxide: Synthesis, Properties, and Applications," *Advanced Materials*, vol. 22, no. 35, pp. 3906–3924, Sep. 2010, doi: 10.1002/adma.201001068.

[3]   J.-H. Chen, C. Jang, S. Xiao, M. Ishigami, and M. S. Fuhrer, "Intrinsic and extrinsic performance limits of graphene devices on SiO2," *Nat Nanotechnol*, vol. 3, no. 4, pp. 206–209, Apr. 2008, doi: 10.1038/nnano.2008.58.

[4]   J. M. Dawlaty *et al.*, "Measurement of the optical absorption spectra of epitaxial graphene from terahertz to visible," *Appl Phys Lett*, vol. 93, no. 13, p. 131905, Sep. 2008, doi: 10.1063/1.2990753.

[5]   F. Xia, T. Mueller, Y. Lin, A. Valdes-Garcia, and P. Avouris, "Ultrafast graphene photodetector," *Nat Nanotechnol*, vol. 4, no. 12, pp. 839–843, Dec. 2009, doi: 10.1038/nnano.2009.292.

[6]   F. H. L. Koppens, T. Mueller, P. Avouris, A. C. Ferrari, M. S. Vitiello, and M. Polini, "Photodetectors based on graphene, other two-dimensional materials and hybrid systems," *Nat Nanotechnol*, vol. 9, no. 10, pp. 780–793, Jan. 2014, doi: 10.1038/NNANO.2014.215.

[7]   S. Schuler *et al.*, "High-responsivity graphene photodetectors integrated on silicon microring resonators," *Nature Communications 2021 12:1*, vol. 12, no. 1, pp. 1–9, Jun. 2021, doi: 10.1038/s41467-021-23436-x.

[8]   G. Konstantatos, "Current status and technological prospect of photodetectors based on two-dimensional materials," *Nature Communications 2018 9:1*, vol. 9, no. 1, pp. 1–3, Dec. 2018, doi: 10.1038/s41467-018-07643-7.

[9]	H. Fang, W. Hu, H. Fang, and W. Hu, "Photogating in Low Dimensional Photodetectors," *Advanced Science*, vol. 4, no. 12, p. 1700323, Dec. 2017, doi: 10.1002/ADVS.201700323.

[10]	L. Turyanska *et al.*, "Ligand-Induced Control of Photoconductive Gain and Doping in a Hybrid Graphene–Quantum Dot Transistor," *Adv Electron Mater*, vol. 1, no. 7, pp. 1–5, 2015, doi: 10.1002/aelm.201500062.

[11]	N. D. Cottam *et al.*, "Defect-assisted high photoconductive UV − Visible gain in perovskite-decorated graphene transistors," *ACS Appl Electron Mater*, vol. 2, no. 1, pp. 147–154, Jan. 2020, doi: 10.1021/ACSAELM.9B00664/ASSET/IMAGES/LARGE/EL9B00664_0006.JPEG.

[12]	N. D. Cottam *et al.*, "Magnetic and electric field dependent charge transfer in perovskite/graphene field effect transistors ," *Adv Electron Mater*, 2022.

[13]	W. Zhang, G. E. Eperon, and H. J. Snaith, "Metal halide perovskites for energy applications," *Nature Energy 2016 1:6*, vol. 1, no. 6, pp. 1–8, May 2016, doi: 10.1038/nenergy.2016.48.

[14]	L. Protesescu *et al.*, "Nanocrystals of Cesium Lead Halide Perovskites (CsPbX3, X = Cl, Br, and I): Novel Optoelectronic Materials Showing Bright Emission with Wide Color Gamut," *Nano Lett*, vol. 15, no. 6, pp. 3692–3696, 2015, doi: 10.1021/nl5048779.

[15]	C. Zhang *et al.*, "Hybrid light emitting diodes based on stable, high brightness all-inorganic CsPbI3 perovskite nanocrystals and InGaN," *Nanoscale*, vol. 11, no. 28, pp. 13450–13457, Jul. 2019, doi: 10.1039/C9NR03707A.

[16]	N. D. Cottam, C. Zhang, J. L. Wildman, A. Patanè, L. Turyanska, and O. Makarovsky, "Light-Induced Stark Effect and Reversible Photoluminescence Quenching in Inorganic Perovskite Nanocrystals," *Adv Opt Mater*, vol. 9, no. 13, Jul. 2021, doi: 10.1002/adom.202100104.

[17]	J. S. Austin *et al.*, "Photosensitisation of inkjet printed graphene with stable all-inorganic perovskite nanocrystals," *Nanoscale*, vol. 15, no. 5, pp. 2134–2142, Feb. 2023, doi: 10.1039/D2NR06429D.

[18]	F. Wang *et al.*, "Inter-Flake Quantum Transport of Electrons and Holes in Inkjet-Printed Graphene Devices," *Adv Funct Mater*, vol. 31, no. 5, p. 2007478, Jan. 2021, doi: 10.1002/adfm.202007478.

[19]	Graphene Supermarket, "Graphene Supermarket: https://www.graphene-supermarket.com/," *https://www.graphene-supermarket.com/*. https://www.graphene-supermarket.com/ (accessed May 30, 2022).

[20]	C. Coletti and V. Miseikis, "CNI@NEST," *NEST*. https://www.iit.it/web/center-for-nanotechnology-innovation (accessed Apr. 05, 2022).

[21]	J. Y. Kim, O. Voznyy, D. Zhitomirsky, and E. H. Sargent, "25th Anniversary Article: Colloidal Quantum Dot Materials and Devices: A Quarter-Century of Advances," *Advanced Materials*, vol. 25, no. 36, pp. 4986–5010, Sep. 2013, doi: 10.1002/ADMA.201301947.

[22]	K. Susumu, B. C. Mei, and H. Mattoussi, "Multifunctional ligands based on dihydrolipoic acid and polyethylene glycol to promote biocompatibility of quantum dots," *Nature Protocols 2009 4:3*, vol. 4, no. 3, pp. 424–436, Mar. 2009, doi: 10.1038/nprot.2008.247.

[23]	L. Turyanska *et al.*, "Tailoring the physical properties of thiol-capped PbS quantum dots by thermal annealing," *Nanotechnology*, vol. 20, no. 31, p. 315604, Jul. 2009, doi: 10.1088/0957-4484/20/31/315604.

[24] L. Wu *et al.*, "Improving the Stability and Size Tunability of Cesium Lead Halide Perovskite Nanocrystals Using Trioctylphosphine Oxide as the Capping Ligand," *Langmuir*, vol. 33, no. 44, pp. 12689–12696, Nov. 2017, doi: 10.1021/ACS.LANGMUIR.7B02963.

[25] D. Yang, X. Li, and H. Zeng, "Surface Chemistry of All Inorganic Halide Perovskite Nanocrystals: Passivation Mechanism and Stability," *Adv Mater Interfaces*, vol. 5, no. 8, p. 1701662, Apr. 2018, doi: 10.1002/ADMI.201701662.

[26] J. Song *et al.*, "Room-Temperature Triple-Ligand Surface Engineering Synergistically Boosts Ink Stability, Recombination Dynamics, and Charge Injection toward EQE-11.6% Perovskite QLEDs," *Advanced Materials*, vol. 30, no. 30, p. 1800764, Jul. 2018, doi: 10.1002/ADMA.201800764.

[27] J. Im *et al.*, "Functionalized Gold Nanoparticles with a Cohesion Enhancer for Robust Flexible Electrodes," *ACS Appl Nano Mater*, vol. 5, no. 5, pp. 6708–6716, May 2022, doi: 10.1021/ACSANM.2C00742/ASSET/IMAGES/MEDIUM/AN2C00742_M001.GIF.

[28] Y. T. Huang *et al.*, "High-Performance InSe Transistors with Ohmic Contact Enabled by Nonrectifying Barrier-Type Indium Electrodes," *ACS Appl Mater Interfaces*, vol. 10, no. 39, pp. 33450–33456, Oct. 2018, doi: 10.1021/ACSAMI.8B10576/ASSET/IMAGES/MEDIUM/AM-2018-105765_0005.GIF.